Intrinsic phonon-limited charge carrier mobilities in thermoelectric SnSe

Jinlong Ma,[1,2] Yani Chen,[1,2] and Wu Li[1,*]

[1]*Institute for Advanced Study, Shenzhen University, Shenzhen 518060, China*

[2]*Key Laboratory of Optoelectronic Devices and Systems of Ministry of Education and Guangdong Province, College of Optoelectronic Engineering, Shenzhen University, Shenzhen 518060, China*

(Received 2 October 2017; revised manuscript received 30 January 2018; published 21 May 2018)

Within the past few years, tin selenide (SnSe) has attracted intense interest due to its remarkable thermoelectric potential for both *n*- and *p*-type crystals. In this work, the intrinsic phonon-limited electron/hole mobilities of SnSe are investigated using a Boltzmann transport equation based on first-principles calculated electron-phonon interactions. We find that the electrons have much larger mobilities than the holes. At room temperature, the mobilities of electrons along the *a*, *b*, and *c* axes are 325, 801, and 623 $cm^2/V\,s$, respectively, whereas those of holes are 100, 299, and 291 $cm^2/V\,s$, respectively. The anisotropy of mobilities is consistent with the reciprocal effective mass at band edges. The mode-specific analysis shows that the highest longitudinal optical phonons, rather than previously assumed acoustic phonons, dominate the scattering processes and consequently the mobilities in SnSe. The room-temperature largest mean free paths of electrons and holes in SnSe are about 21 and 13 nm, respectively.

DOI: 10.1103/PhysRevB.97.205207

I. INTRODUCTION

Thermoelectric materials can directly convert the heat into power, which is of great significance for energy harvesting. The conversion efficiency of thermoelectric materials is characterized by the dimensionless figure of merit $ZT = \frac{S^2\sigma T}{\kappa}$, where S is the Seebeck coefficient, σ is the electrical conductivity, T is the temperature, and κ is the thermal conductivity. Exploration of high ZT materials is still ongoing and new thermoelectric materials are continuously emerging [1–4]. The strategies to increase ZT mainly focused on enhancing the power factor $S^2\sigma$, for instance, through band-structure engineering [5,6] or reducing the lattice thermal conductivity through alloying and nanostructuring [7–10]. Screening from pristine compounds with intrinsically low thermal conductivity such as clathrates [11] and oxyselenides [12] is another important trend. These types of materials, however, are heavy-metal-based systems containing rare-earth and low-abundance elements.

Recently single-crystal SnSe, a layered material, has attracted intense attention for its high ZT, which is mainly attributed to the intrinsically low thermal conductivity. In 2014, Zhao *et al.* [13] found an unprecedented high ZT of about 2.6 at 923 K in unintentionally doped *p*-type SnSe along the *b*-axis direction, while ZT can reach as high as 2.3 and 0.8 along the *c* and *a* axes, respectively. Later, an increased ZT ranging from 0.7 to 2.0 was obtained in the Na-doped *p*-type SnSe along the *b* axis at moderate temperatures from 300 to 773 K [14]. For thermoelectric device applications, it is also necessary to have *n*-type SnSe with comparable ZT. Duong *et al.* [15] successfully synthesized *n*-type SnSe via Bi doping, and a maximum ZT of 2.2 was achieved at 733 K in the highly doped samples also along the *b* axis. Therefore, SnSe is a robust candidate with high efficiency ready for thermoelectric devices in a broad temperature range.

The ZT of single-crystal SnSe shows strong anisotropy. The highest ZT was always observed along the *b* axis, whereas ZT along the *c* axis was slightly smaller and the *a* axis displays much smaller ZT than the other two axes [13–15]. The seebeck coefficient shows weak anisotropy, especially in *p*-type samples [13–15], and therefore the anisotropy of ZT is mainly due to the anisotropy of thermal and electrical transport properties. The room-temperature thermal conductivity measured in Ref. [13] reaches as low as 0.47, 0.68, and 0.70 W/mK along *a*, *b*, and *c* axes, respectively, which are surprisingly lower than those in polycrystals [16,17]. It was pointed out in a comment by Wei *et al.* [18] that the density of the samples used in Ref. [13] was only 88–90% of the theoretical density. Very recently, two to three times larger thermal conductivities with marked anisotropy between *b* and *c* axes were reported for high-quality single crystalline SnSe [19], in agreement with the first-principles calculations [20,21]. Despite intense studies of intrinsic thermal conductivity of SnSe, intrinsic charge carrier transport properties, which are limited by phonon scattering, remain little known, especially theoretically. Conventional studies of electrical transport rely on many approximations such as perfectly parabolic band structure and fitted relaxation times [21–25]. Very recently, the fully parameter-free calculation of electrical transport properties of semiconductors has been enabled by solving the Boltzmann transport equation (BTE) combined with interpolated electron-phonon coupling matrix based on first-principles calculations [26–34].

In this study, the electron and hole mobilities of thermoelectric SnSe are investigated by solving BTE with Wannier function interpolation of first-principles calculated electron-phonon coupling matrix [35]. It is found that the electrons mobilities are few times larger than holes and that the mobilities display evident anisotropy. The mode-specific analysis of scattering rates and mean free paths (MPFs) is also made. The

*wu.li.phys2011@gmail.com

highest longitudinal-optical phonons dominate the transport properties.

II. METHODOLOGY

The electrical conductivity tensor can be calculated from the solution of BTE. At temperature T, it is formulated as [26]

$$\sigma^{\alpha\beta} = \frac{2q^2}{NVk_BT}\sum_{n\mathbf{k}} f^0_{n\mathbf{k}}\left(1 - f^0_{n\mathbf{k}}\right)v^\alpha_{n\mathbf{k}}F^\beta_{n\mathbf{k}}, \quad (1)$$

where $n\mathbf{k}$ indicates the electron states with band index n and wave vector $\mathbf{k}$. q is the elementary charge, k_B is the Boltzmann constant, N is the number of uniformly sampled $\mathbf{k}$ points in the Brillouin zone, V is the volume of unit cell, α and β are Cartesian directions. $f^0_{n\mathbf{k}}$ is the equilibrium Fermi-Dirac distribution, $v^\alpha_{n\mathbf{k}}$ is the electron velocity along the α direction, $F^\beta_{n\mathbf{k}}$ is the mean free displacement projected in the β direction, which can be calculated from the iterative solution of BTE starting with the relaxation time approximation (RTA) solution $\mathbf{F}^{\mathrm{RTA}}_{n\mathbf{k}} = \mathbf{v}_{n\mathbf{k}} \cdot \tau_{n\mathbf{k}}$. The intrinsic relaxation time $\tau_{n\mathbf{k}}$ is limited by electron-phonon coupling [26,34]. The mobility is then obtained from

$$\mu^{\alpha\beta} = \frac{\sigma^{\alpha\beta}}{n_c q}, \quad (2)$$

where n_c is carrier density, which can be calculated with $n_c = \frac{2}{NV}\sum_{n\mathbf{k}} f^0_{n\mathbf{k}}$ and $n_c = \frac{2}{NV}\sum_{n\mathbf{k}}(1 - f^0_{n\mathbf{k}})$ for electrons and holes, respectively.

The *Pnma* phase SnSe has an anisotropic layered orthorhombic crystal structure [20,21], as shown in Fig. 1. The density functional theory (DFT) calculations were performed by using QUANTUM ESPRESSO (QE) [36] with Perdew-Burke-Ernzerhof (PBE) exchange-correlation functional [37]. The experimental structure including lattice constants of $a = 11.501$ Å, $b = 4.153$ Å, and $c = 4.445$ Å and atomic coordinates was used in the calculation [22,38]. The one-shot GW calculation of band structure was performed by using BerkeleyGW [39]. The EPW package [35] was employed for Wannier function interpolation of electronic band structure, phonon dispersion, and electron-phonon coupling matrix with

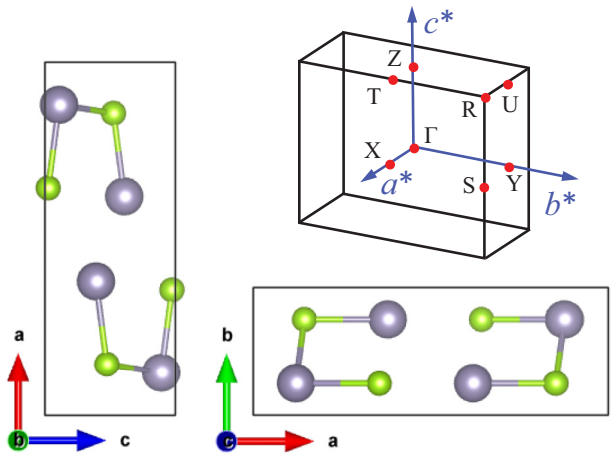

FIG. 1. Crystal structure of *Pnma* phase SnSe (gray: Sn atoms; green: Se atoms) and correspondingly the first Brillouin zone with high-symmetry points.

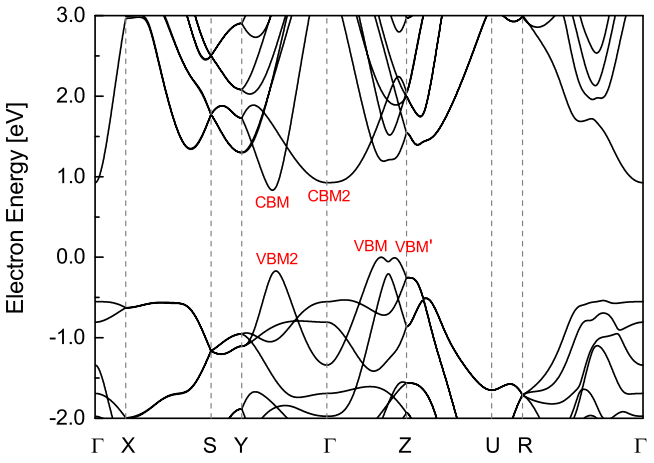

FIG. 2. Electronic band structure of SnSe with GW calculation along high-symmetry directions.

initial $3 \times 6 \times 6$ $\mathbf{k}$ and $\mathbf{q}$ grids, dense enough to ensure the accuracy of Wannier function interpolation [22].

III. RESULTS AND DISCUSSIONS

Figure 2 shows the calculated electronic band structure of SnSe along high-symmetry directions. The calculated band gap is 0.833 eV, in good agreement with the experimental values of 0.82–0.923 eV [13,40–42] and previous GW calculation of 0.829 eV [22]. The valence-band maximum (VBM) valley locates in the Γ-Z direction, and a local valence maximum (VBM′) exists very close to VBM, as revealed in previous calculations [22,23,43,44]. These so-called "pudding-mold-like" shape valence-band maxima have been confirmed by angle-resolved photoemission spectroscopy (ARPES) measurement recently [45–47]. The effective mass m^* of these two maxima along different directions are calculated. The effective masses of the VBM valley are 0.68, 0.33, and $0.15m_0$ along a, b, and c axes, respectively, while they are 0.85, 0.13, and $0.14m_0$ for the VBM′ valley, in agreement with previous calculations [22,45]. The a-axis effective mass in these two valleys is always the largest. Another local valence-band maximum (VBM2) valley appears 0.17 eV below the VBM. The conduction-band minimum (CBM) valley lies in the Γ-Y direction, and the other local conduction-band minimum (CBM2) valley is about 0.09 eV higher than the CBM. The effective masses of the CBM valley are 1.84, 0.10, and $0.14m_0$ along a, b, and c axes, respectively.

Due to the fact that BerkeleyGW does not support the spin-obit coupling (SOC) calculation using QE [36], the SOC was not included in the QE calculation. We have performed extra DFT calculations using VASP. We shift the valence and conduction bands obtained from VASP with and without SOC separately so that VBM and CBM coincide with those obtained from QE without SOC. As shown in Fig. 3, the band structure close to the band edges, which are relevant for transport properties, are almost the same from QE and VASP and are almost unaffected by the SOC. This indicates that our QE calculations without including SOC should be reliable.

Reference [48] found that PBE leads to systematic underestimation of phonon frequencies for SnSe and local density approximation (LDA) can give better agreement with

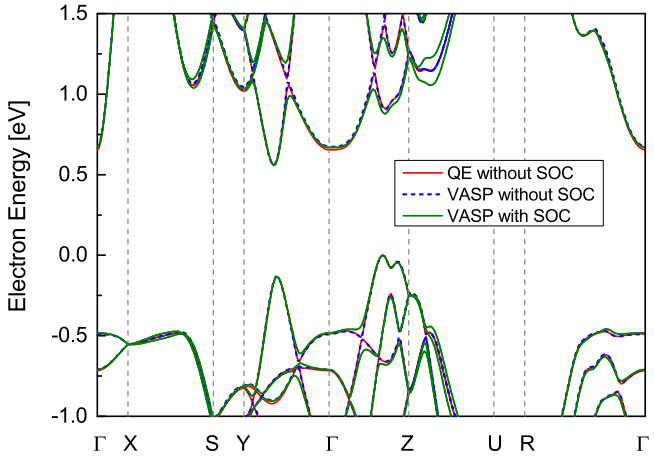

FIG. 3. Electronic band structure of SnSe calculated with and without SOC. The valence and conduction bands obtained from VASP with and without SOC were shifted separately so that the VBM and CBM coincide with those obtained from QE without SOC.

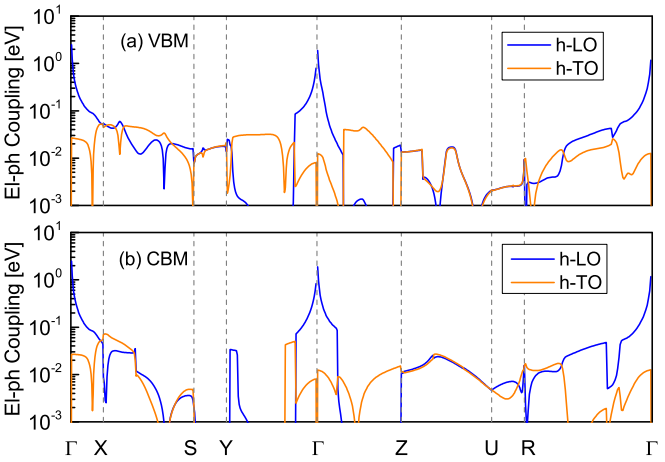

FIG. 5. Calculated electron-phonon coupling elements of (a) initial VBM and (b) initial CBM electron with the highest LO and TO phonons along high-symmetry directions.

experiments. We find this is actually due to the overestimation of lattice constants in the ground-state calculation using PBE. From PBE, the relaxed structure gives lattice constants $a = 11.718$ Å, $b = 4.209$ Å, and $c = 4.493$ Å, about 2% larger than the experimental values. The corresponding phonon dispersion is plotted in Fig. 4, showing about 15% underestimation as compared to experiments. However, when using experimental lattice parameters, PBE can reproduce experimental phonon dispersion as satisfactorily as LDA does in Ref. [48]. The longitudinal-transverse optical (LO-TO) splitting is calculated by including the long-range Coulomb interactions with the nonanalytic correction term from dielectric constant and Born effective charges [36]. By comparing to the phonon dispersion without including LO-TO splitting, we found that the long-range Coulomb interactions have a much stronger effect on the highest LO (h-LO) phonons than other branches. The stronger effect is also reflected in the electron-phonon coupling strength, as shown in Fig. 5. This long-range polar effect on the electron-phonon coupling is considered by using the polar Wannier function interpolation scheme [32–34], unifying the treatments of nonpolar and polar systems in a convenient calculational framework and implemented in the EPW package [35]. It can be seen that the coupling elements of VBM and CBM electrons with the polar h-LO phonons diverge with decreasing phonon wave vector as expected [35,50,51], and are orders of magnitudes larger than those with the highest TO (h-TO) phonons. The electron-phonon coupling elements of other phonon branches could not be well separated and are as small as the h-TO phonons.

For mobility calculation, the related quantities were interpolated to dense grids and the same final grid was used for **k** and **q**. The convergence test with respect to the final grid was carefully checked, as shown in Fig. 6. The $36 \times 96 \times 96$ **k** and **q** sampling was used for the results presented hereafter. The chemical potential is chosen to be 0.3 eV away from the band edge and in the band gap, so that it corresponds to low doping limit, where the defect scattering can be ignored. As long as

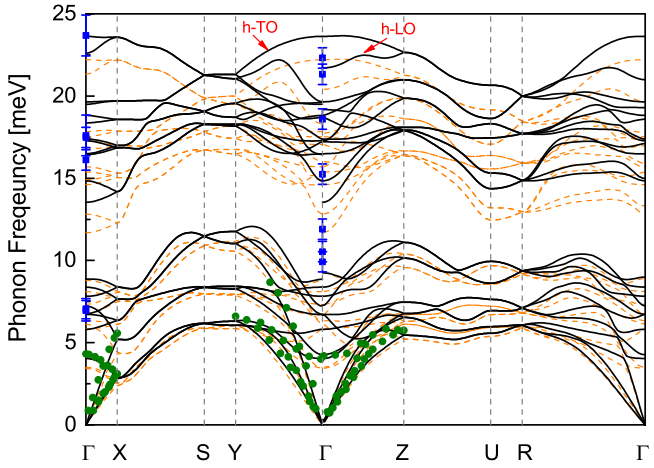

FIG. 4. Phonon dispersion of SnSe along high-symmetry directions calculated with relaxed structure (dashed line) and experimental structure (solid line), compared with the experimental data from Ref. [48] (circles) and Ref. [49] (squares).

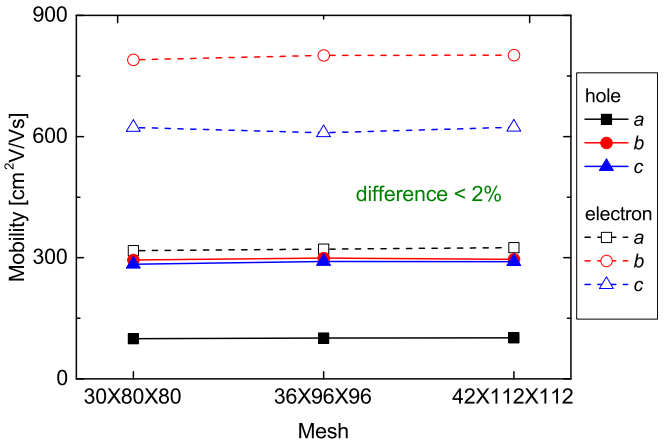

FIG. 6. Convergence test of the room-temperature hole and electron mobilities of SnSe along a, b, and c axes with respect to the **k** and **q** mesh.

TABLE I. Calculated room-temperature hole mobilities μ along a, b, and c axes and hole concentration n_c corresponding to different chemical potentials relative to the valence-band maximum.

Chemical potential (eV)	μ^a (cm^2/Vs)	μ^b (cm^2/Vs)	μ^c (cm^2/Vs)	n_c (cm^{-3})
0.10	99.5	293.9	283.1	3.56×10^{17}
0.20	99.8	294.2	283.9	7.49×10^{15}
0.30	99.8	294.2	283.9	1.57×10^{14}

the chemical potential is far enough away in the band gap from the band edges, it only affects the carrier concentration but not the scattering rates. In this case, the mobility no longer depends on the concentration, as can be seen from Table I. The calculated mobility corresponds to intrinsic phonon-limited mobility measured at the low concentration limit [34].

Figure 7 shows the calculated hole mobilities of SnSe along a, b, and c axes, compared with the experimental measurements in the b-c plane [42,52–54] and along each axis [13]. At room temperature, the calculated mobilities are 100, 299, and 291 cm^2/V s along a, b, and c axes, respectively. For comparison, the RTA results are also plotted, which show significant underestimations. For instance, room-temperature underestimation is about 50%, 31%, and 34% for a, b, and c axes, respectively, indicating the importance of the exact solution of BTE in the calculation of intrinsic mobility of SnSe. The underestimation is primarily attributed to the intravalley scattering by polar LO phonons [34,55]. The transition rates are proportional to the squared coupling matrix elements $|g|^2$ and the phonon occupation number $N_{\mathbf{q}}$ [26]. For those long-wavelength acoustic phonons involved in the scattering, $|g|^2$ and $N_{\mathbf{q}}$ are proportional and inversely proportional to $|\mathbf{q}|$, respectively. As a result, the intravalley acoustic-phonon scattering is almost isotropic with respect to the direction of $\mathbf{q}$. The intravalley scattering by nonpolar optical phonons is isotropic as well. The intervalley scattering is symmetric due

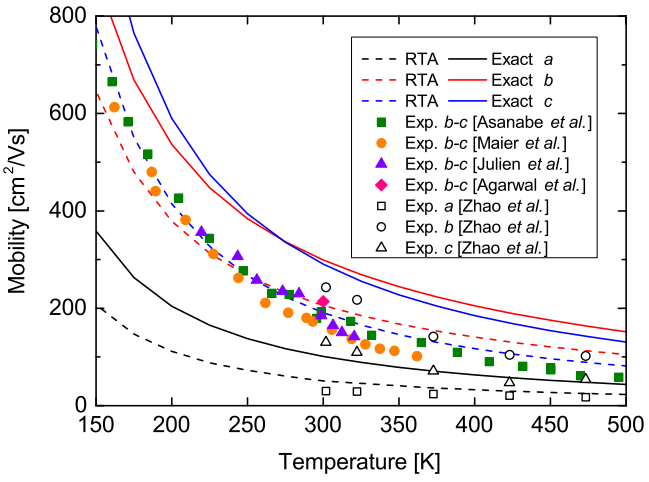

FIG. 7. Calculated hole mobilities of SnSe along different directions from RTA (dashed lines) and exact solution (solid lines) of BTE. The solid symbols are experimental data in the b-c plane from Refs. [52,53,54,42], while the open symbols are experimental values along each directions from Ref. [13]. The measured a-axis mobility is almost vanishing in Ref. [42] and is thus not plotted.

to symmetries of the structure. However, the electron-phonon coupling matrix elements of polar LO phonons is divergent around the Γ point, and thus the transition rates to different final electron states are very sensitive to the direction of $\mathbf{q}$ and determine the $|\mathbf{q}|$ involved. As a consequence, unlike in other intravalley and intervalley scatterings, the forward scattering due to the intravalley LO phonons cannot cancel out with the backward scattering, so the extra term in the linearized BTE cannot be neglected [33,34,55]. At high temperatures, the relative contribution to the mobility from high-energy carriers increases. Considering that the contribution of LO phonons to the scattering of high-energy carriers decreases, as in the case of GaAs [33,34] and will be shown in Fig. 9, the difference between RTA and exact solution of BTE is reduced. It is therefore expected that the RTA underestimation could be less significant for intermediate- and high-temperature phases. The calculated mobilities show a $T^{-1.5\text{–}1.8}$ temperature dependence, while the measured temperature dependence of single-crystal SnSe is $T^{-2.0\text{–}2.4}$ in the b-c plane [40,52–54], $T^{-1.3}$ for the a axis, and $T^{-2.7}$ for the b and c axes around room temperature in Ref. [13]. The measured mobilities for polycrystal SnSe roughly depends on $T^{-1.5}$ in the range of 400–600 K [16,56].

The calculated mobilities are larger than the experimental values. Two factors can account for the discrepancy. The first is the defect scattering, which was not taken into account in the calculation. For instance, the Sn vacancy has been found to be the intrinsic acceptor defect in SnSe [57]. As temperature increases, the defect scattering should become relatively weak, and phonon scattering dominates. Thus, the relative deviation from experimental values decreases, as can be seen in the a-axis mobilities. Second, a Hall factor r_H of unity was assumed when extracting the carrier concentration n_c from Hall measurements, which is needed to calculate the mobility. However, r_H depends on magnetic field, temperature, and doping. It becomes unity only in the case of parabolic and isotropic band and constant relaxation time. Although n_c should be independent of orientation, the n_c of SnSe extracted in the experiments varies by up to three times with the orientation [13], implying that r_H actually deviates from unity significantly. We note that μ^b and μ^c extracted from experiments do not decrease monotonically with T, which should be related to the error in r_H. Our calculation shows that the mobilities along b and c axes are similar and that the sequence that they follow is reversed at 275 K. The σ^c measured in Ref. [13] is slightly larger than σ^b between 300 and 500 K. However due to the fact that the n_c extracted for the c axis is almost two times larger than that for the b axis, the reported μ^c is much lower than μ^b [13]. Though there exists discrepancy regarding which direction has the largest μ [13,19,52], μ^a seems to be always the smallest. At the room temperature, the measured anisotropy ranges from 3.7 to 7.7 in Refs. [13,19,52,58] and even 4.66×10^4 in Ref. [42]. The largest anisotropy at room temperature in our calculation is about 3. The RTA overestimates the anisotropy, and gives 4.1. Other calculations based on RTA and other approximations obtained anisotropy in the range from 1.5 to 4.4 at room temperature [21,22,59].

The anisotropy of mobility to some extent can be reflected in the anisotropy of the average velocity. Figure 8 shows the average velocity at different energies, calculated as

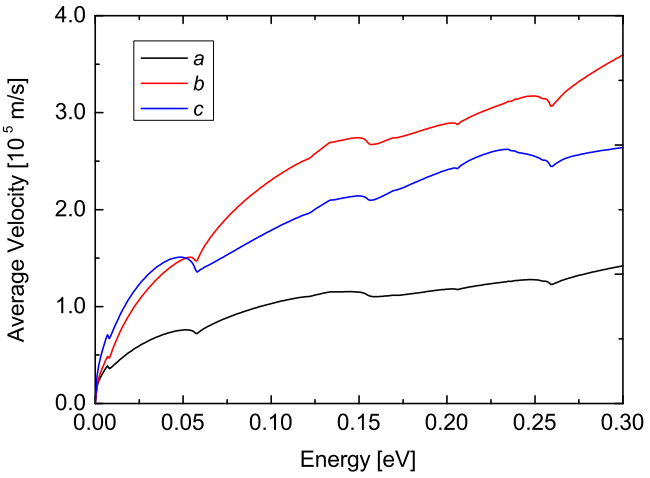

FIG. 8. Average hole velocity of SnSe along different directions.

$\bar{v}^\alpha(\epsilon) = \sqrt{\sum_{n\mathbf{k}} |v^\alpha_{n\mathbf{k}}|^2 \delta(\epsilon - \epsilon_{n\mathbf{k}}) / \sum_{n\mathbf{k}} \delta(\epsilon - \epsilon_{n\mathbf{k}})}$, with $\epsilon_{n\mathbf{k}}$ being electron energy at state $n\mathbf{k}$. The $\bar{v}^a$ is always the smallest below 0.3 eV, due to the highest effective mass along the a-axis direction. It is interesting that $\bar{v}^b$ and $\bar{v}^c$ cross at 0.05 eV, due to the change of effective masses between VBM and VMB′ valley. The relative contribution from high-energy carriers to the mobility increases with increasing temperature. Since the anisotropy between the b and c axes contributed from high-energy holes cancels out that from low-energy ones at high temperatures, the anisotropy within the b-c plane decreases and even has a reversion at relatively high temperature. The $\bar{v}^b/\bar{v}^a$ increases with increasing energy, consistent with increasing μ^b/μ^a. The $\bar{v}^c/\bar{v}^a$ shows a weak dependence on energy which can also explain the almost temperature-independent μ^c/μ^a.

In polar materials, scattering from LO phonons is important and even can be dominant [32–34]. Figure 9(a) shows the total scattering rates of holes and the contributions from h-LO phonons in SnSe at room temperature. At relatively low energies, the h-LO phonons dominate the scattering processes; for instance, below 0.10 eV, about 57–75% of the scattering rates are contributed by h-LO phonons, while the other phonons dominate at higher energies. Considering 85–90% of the mobility is contributed from holes with energy smaller than 0.10 eV, the h-LO phonons hence dominate the mobility. Therefore, the assumption that acoustic phonons limit the scattering processes made in Ref. [21] is not very accurate. The scattering rate has an obvious jump around 20 meV, corresponding to the frequency of h-LO phonon at the Brillouin-zone center. This jump is due to the occurrence of h-LO phonon emission processes [26,32–34]. Figure 9(b) shows the MPFs, defined as $\Lambda_{n\mathbf{k}} = |\mathbf{F}^{\mathrm{RTA}}_{n\mathbf{k}}|$, of holes at room temperature. The MFPs are quite scattered due to strong anisotropy of the system. One peak appears at 20 meV, corresponding to the onset of h-LO phonon emission scattering. The largest hole MFP is about 13 nm at room temperature.

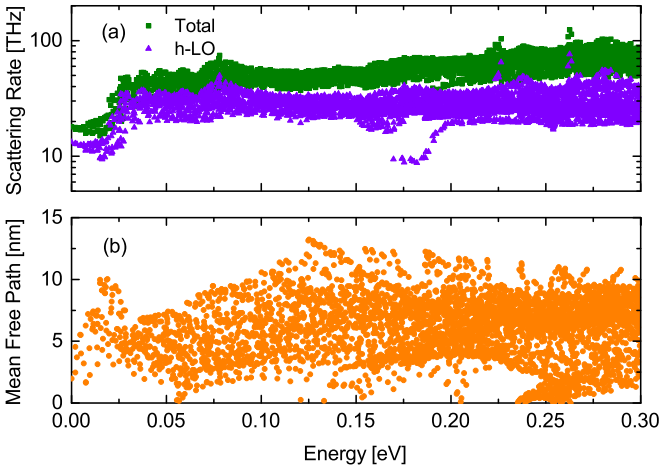

FIG. 9. (a) Total scattering rates along with the contributions from h-LO phonons, and (b) mean free paths of holes in SnSe at room temperature.

We also studied the Seebeck coefficient [28,60],

$$S^{\alpha\beta} = \frac{2q(\sigma^{\alpha\gamma})^{-1}}{NVk_{\mathrm{B}}T^2} \sum_{n\mathbf{k}} f^0_{n\mathbf{k}}\left(1 - f^0_{n\mathbf{k}}\right)(\epsilon_{n\mathbf{k}} - \epsilon_0) v^\gamma_{n\mathbf{k}} F^\beta_{n\mathbf{k}}, \quad (3)$$

where ϵ_0 is the chemical potential. The chemical potential is adjusted such that the hole concentration is equal to the mean value of the experimental concentrations in the three principal directions extracted for Hall measurements in Ref. [13], as shown in Fig. 10(a). The calculated Seebeck coefficients agree with the experiments within 10% [Fig. 10(b)]. The Seebeck coefficient can be decomposed into a scattering term and a band term [21,61,62]. The band term is determined by the band structure alone, which can be obtained from a constant relaxation time approximation (CRTA) [60]. We find that the difference between the CRTA and the exact solution of BTE is smaller than 5%. Our calculated band term agrees with the calculations in Ref. [57]. It was also found there that the calculated Seebeck coefficients can agree well with experiments at intermediate and high temperatures if further considering the temperature effect on the structure [57]. We also notice that unlike the mobility, the Seebeck coefficient

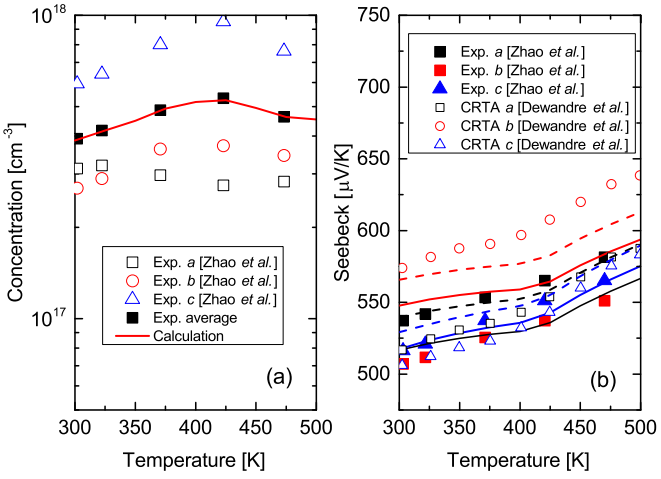

FIG. 10. (a) Temperature dependence of the hole concentration compared with experiments. (b) Calculated Seebeck coefficient of SnSe, where the solid symbols are experimental data from Zhao *et al.* [13], the open symbols are CRTA calculations from Dewandre *et al.* [57], the dashed and solid lines are CRTA and exact solution of BTE in this work, respectively.

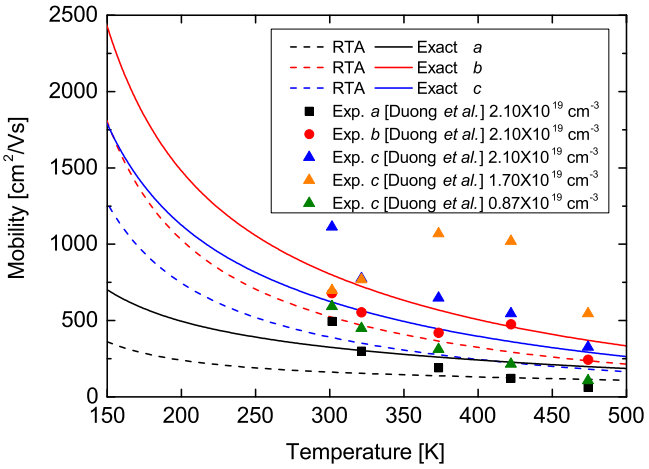

FIG. 11. Electron mobilities of SnSe in different directions from RTA (dashed line) and exact solution (solid lines) of BTE. The symbols are experimental data derived from electrical conductivity and carrier concentration from Ref. [15].

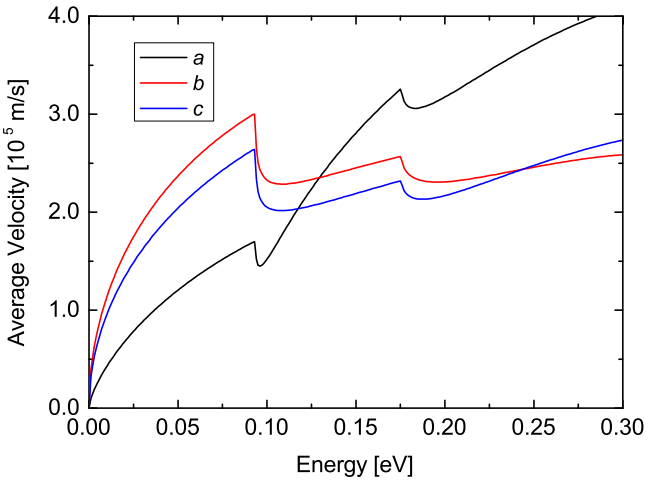

FIG. 12. Average electron velocity of SnSe along different directions.

under RTA agrees with the exact solution of BTE within 2% in the whole temperature range considered, since it is almost exclusively dominated by the band term.

Figure 11 shows the calculated electron mobilities of SnSe along different directions, which also have evident anisotropy. At room temperature, the mobilities are 325, 801, and 623 $cm^2/V\,s$ along a, b, and c axes, respectively. The RTA solution underestimates the electron mobilities, for instance, at room temperature the underestimations are about 50%, 35%, and 37% along a, b, and c axes directions, respectively. The temperature dependence of electron mobility follows $T^{-1.3–1.6}$. For comparison, we also plotted the mobilities derived from the measured electrical conductivity and carrier concentration of heavily doped SnSe in Ref. [15]. The calculated intrinsic mobility deviates significantly from the measurements for heavily doped samples. We also note that the measurements showed that the mobility even increases with doping.

Similar to the hole, the calculated a-axis mobility of the electron is the smallest, whereas the largest mobility is in the b-axis direction, consistent with previous estimation [21] and the anisotropy of the low-energy velocity $\bar{v}^a < \bar{v}^c < \bar{v}^b$, as shown in Fig. 12. The anisotropy of the low-energy velocity is related to that of m^* for the CBM valley $m^{*,a} > m^{*,c} > m^{*,b}$. The velocity of the high-energy electrons follows the sequence opposite to the low-energy electrons. As a result, the anisotropy of μ among the a, b, and c axes decreases as the temperature increases. In contrast to the sequence of mobility from the calculations, the measured conductivity along the c axis is larger than along the b axis in the same heavily doped sample [15]. This might be due to the heavy doping to achieve n-type SnSe, whereas the naturally grown SnSe is p type. The heavy doping possibly changes the band structure and enhances the effective mass, which are generally not considered in first-principles calculations [45]. The enhancements along different directions are not homogeneous, and the sequence of effective masses as compared to the intrinsic case can even be reversed, as discovered in p-type SnSe [14,45]. We also notice that the sequence that the b- and c-axis conductivities followed was reversed in Na-doped p-type SnSe as compared to the as-grown p-type SnSe [13,14].

Figure 13 shows the scattering rates and MFPs of electrons at room temperature. The scattering rates in the CBM valley show very weak anisotropy up to 0.09 eV, where the CBM2 appears. The h-LO phonons also contribute dominantly to the scattering rates of electrons at low energies, about 55–72% below 0.09 eV. The electrons in this energy range contribute about 75–85% to the mobility. Because of the emission processes of h-LO phonons, the jump of scattering rates also appears around 20 meV for electrons in SnSe. The largest MFP is about 21 nm at room temperature, as shown in Fig. 13(b). The MFPs of phonons dominating the lattice thermal conductivity are of the same order of magnitude as charge carriers. Phonons with MFPs smaller than 30 nm contribute over 95% to the thermal conductivity at room temperature [21], indicating that the nanostructuring can hardly cause noticeable improvement in the thermoelectric properties of SnSe.

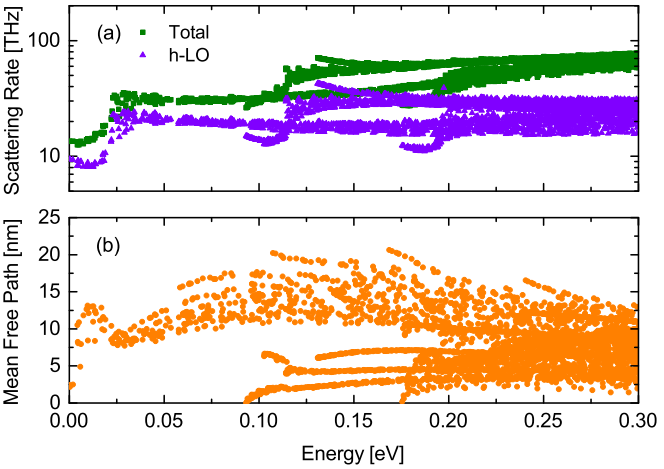

FIG. 13. (a) Total scattering rates along with the contributions from h-LO phonons, and (b) mean free path of electrons in SnSe at room temperature.

IV. CONCLUSIONS

In summary, we performed a fully first-principles calculations of the mobilities for both electrons and holes in thermoelectric SnSe at the low-temperature *Pmna* phase by solving BTE combined with Wannier function interpolation of electron-phonon coupling matrix. Electrons have much larger mobilities than holes. The mobilities of electrons and holes display evident and different anisotropy, consistent with the reciprocal effective mass at band edges. The polar effect is important in SnSe, and the highest longitudinal optical phonons, rather than acoustic phonons, dominate the scattering processes and mobilities. At room temperature, the largest mean free paths are about 21 and 13 nm for electrons and holes, respectively. In addition, relaxation time approximation significantly underestimates the mobility of *Pmna* phase SnSe, and for the Seebeck coefficient, it is verified that constant relaxation time approximation works excellently in SnSe.

ACKNOWLEDGMENTS

We acknowledge support from the Natural Science Foundation of China under Grant No. 11704258, the Natural Science Foundation of Guangdong Province under Grant No. 2017A030310377, and the Natural Science Foundation of Shenzhen City under Grant No. JCYJ20170412105922384. J.M. also acknowledges support from the China Postdoctoral Science Foundation under Grant No. 2017M612707.

[1] G. J. Snyder and E. S. Toberer, Nat. Mater **7**, 105 (2008).
[2] P. Sundarraj, D. Maity, S. S. Roy, and R. A. Taylor, RSC Adv. **4**, 46860 (2014).
[3] X. Zhang and L.-D. Zhao, J. Materiomics **1**, 92 (2015).
[4] G. Tan, L.-D. Zhao, and M. G. Kanatzidis, Chem. Rev. **116**, 12123 (2016).
[5] Y. Pei, H. Wang, and G. J. Snyder, Adv. Mater. **24**, 6125 (2012).
[6] A. M. Dehkordi, M. Zebarjadi, J. He, and T. M. Tritt, Mater. Sci. Eng. R **97**, 1 (2015).
[7] J.-F. Li, W.-S. Liu, L.-D. Zhao, and M. Zhou, NPG Asia Mater. **2**, 152 (2010).
[8] W. Liu, X. Yan, G. Chen, and Z. Ren, Nano Energy **1**, 42 (2012).
[9] A. I. Hochbaum, R. Chen, R. D. Delgado, W. Liang, E. C. Garnett, M. Najarian, A. Majumdar, and P. Yang, Nature (London) **451**, 163 (2008).
[10] A. I. Boukai, Y. Bunimovich, J. Tahir-Kheli, J.-K. Yu, W. A. Goddard III, and J. R. Heath, Nature (London) **451**, 168 (2008).
[11] H. Kleinke, Chem. Mater. **22**, 604 (2010).
[12] L.-D. Zhao, J. He, D. Berardan, Y. Lin, J.-F. Li, C.-W. Nan, and N. Dragoe, Energy Environ. Sci. **7**, 2900 (2014).
[13] L.-D. Zhao, S.-H. Lo, Y. Zhang, H. Sun, G. Tan, C. Uher, C. Wolverton, V. P. Dravid, and M. G. Kanatzidis, Nature (London) **508**, 373 (2014).
[14] L.-D. Zhao, G. Tan, S. Hao, J. He, Y. Pei, H. Chi, H. Wang, S. Gong, H. Xu, V. P. Dravid, C. Uher, G. J. Snyder, C. Wolverton, and M. G. Kanatzidis, Science **351**, 141 (2016).
[15] A. T. Duong, V. Q. Nguyen, G. Duvjir, V. T. Duong, S. Kwon, J. Y. Song, J. K. Lee, J. E. Lee, S. Park, T. Min, J. Lee, J. Kim, and S. Cho, Nat. Commun. **7**, 13713 (2016).
[16] C.-L. Chen, H. Wang, Y.-Y. Chen, T. Day, and G. J. Snyder, J. Mater. Chem. A **2**, 11171 (2014).
[17] S. Sassi, C. Candolfi, J.-B. Vaney, V. Ohorodniichuk, P. Masschelein, A. Dauscher, and B. Lenoir, Appl. Phys. Lett. **104**, 212105 (2014).
[18] P.-C. Wei, S. Bhattacharya, J. He, S. Neeleshwar, R. Podila, Y. Y. Chen, and A. M. Rao, Nature (London) **539**, E1 (2016).
[19] D. Ibrahim, J.-B. Vaney, S. Sassi, C. Candolfi, V. Ohorodniichuk, P. Levinsky, C. Semprimoschnig, A. Dauscher, and B. Lenoir, Appl. Phys. Lett. **110**, 032103 (2017).
[20] J. Carrete, N. Mingo, and S. Curtarolo, Appl. Phys. Lett. **105**, 101907 (2014).
[21] R. Guo, X. Wang, Y. Kuang, and B. Huang, Phys. Rev. B **92**, 115202 (2015).
[22] G. Shi and E. Kioupakis, J. Appl. Phys. **117**, 065103 (2015).
[23] K. Kutorasinski, B. Wiendlocha, S. Kaprzyk, and J. Tobola, Phys. Rev. B **91**, 205201 (2015).
[24] Y. Suzuki and H. Nakamura, Phys. Chem. Chem. Phys. **17**, 29647 (2015).
[25] Y. Zhang, S. Hao, L.-D. Zhao, C. Wolverton, and Z. Zeng, J. Mater. Chem. A **4**, 12073 (2016).
[26] W. Li, Phys. Rev. B **92**, 075405 (2015).
[27] F. Giustino, Rev. Mod. Phys. **89**, 015003 (2017).
[28] B. Qiu, Z. Tian, A. Vallabhaneni, B. Liao, J. M. Mendoza, O. D. Restrepo, X. Ruan, and G. Chen, Europhys. Lett. **109**, 57006 (2015).
[29] J. Zhou, B. Liao, B. Qiu, S. Huberman, K. Esfarjani, M. S. Dresselhaus, and G. Chen, Proc. Natl. Acad. Sci. U.S.A. **112**, 14777 (2015).
[30] M. Fiorentini and N. Bonini, Phys. Rev. B **94**, 085204 (2016).
[31] B. Liao, J. Zhou, B. Qiu, M. S. Dresselhaus, and G. Chen, Phys. Rev. B **91**, 235419 (2015).
[32] J.-J. Zhou and M. Bernardi, Phys. Rev. B **94**, 201201(R) (2016).
[33] T.-H. Liu, J. Zhou, B. Liao, D. J. Singh, and G. Chen, Phys. Rev. B **95**, 075206 (2017).
[34] J. Ma, A. S. Nissimagoudar, and W. Li, Phys. Rev. B **97**, 045201 (2018).
[35] S. Poncé, E. Margine, C. Verdi, and F. Giustino, Comput. Phys. Commun. **209**, 116 (2016).
[36] P. Giannozzi, S. Baroni, N. Bonini, M. Calandra, R. Car, C. Cavazzoni, D. Ceresoli, G. L. Chiarotti, M. Cococcioni, I. Dabo, A. D. Corso, S. de Gironcoli, S. Fabris, G. Fratesi, R. Gebauer, U. Gerstmann, C. Gougoussis, A. Kokalj, M. Lazzeri, L. Martin-Samos *et al.*, J. Phys.: Condens. Matter **21**, 395502 (2009).
[37] J. P. Perdew, K. Burke, and M. Ernzerhof, Phys. Rev. Lett. **77**, 3865 (1996).
[38] T. Chattopadhyay, J. Pannetier, and H. V. Schnering, J. Phys. Chem. Solids **47**, 879 (1986).
[39] J. Deslippe, G. Samsonidze, D. A. Strubbe, M. Jain, M. L. Cohen, and S. G. Louie, Comput. Phys. Commun. **183**, 1269 (2012).
[40] J. Yu, A. Yue, and O. Stafsudd, J. Cryst. Growth **54**, 248 (1981).
[41] M. Parenteau and C. Carlone, Phys. Rev. B **41**, 5227 (1990).
[42] A. Agarwal, J. Cryst. Growth **183**, 347 (1998).

[43] L.-D. Zhao, C. Chang, G. Tan, and M. G. Kanatzidis, Energy Environ. Sci. **9**, 3044 (2016).
[44] R. L. Gonzalez-Romero, A. Antonelli, and J. J. Melendez, Phys. Chem. Chem. Phys. **19**, 12804 (2017).
[45] Q. Lu, M. Wu, D. Wu, C. Chang, Y.-P. Guo, C.-S. Zhou, W. Li, X.-M. Ma, G. Wang, L.-D. Zhao, L. Huang, C. Liu, and J. He, Phys. Rev. Lett. **119**, 116401 (2017).
[46] C. W. Wang, Y. Y. Y. Xia, Z. Tian, J. Jiang, B. H. Li, S. T. Cui, H. F. Yang, A. J. Liang, X. Y. Zhan, G. H. Hong, S. Liu, C. Chen, M. X. Wang, L. X. Yang, Z. Liu, Q. X. Mi, G. Li, J. M. Xue, Z. K. Liu, and Y. L. Chen, Phys. Rev. B **96**, 165118 (2017).
[47] Z. Wang, C. Fan, Z. Shen, C. Hua, Q. Hu, F. Sheng, Y. Lu, H. Fang, Z. Qiu, J. Lu, Z. Liu, W. Liu, Y. Huang, Z.-A. Xu, D. W. Shen, and Y. Zheng, Nat. Commun. **9**, 47 (2018).
[48] D. Bansal, J. Hong, C. W. Li, A. F. May, W. Porter, M. Y. Hu, D. L. Abernathy, and O. Delaire, Phys. Rev. B **94**, 054307 (2016).
[49] H. R. Chandrasekhar, R. G. Humphreys, U. Zwick, and M. Cardona, Phys. Rev. B **15**, 2177 (1977).
[50] C. Verdi and F. Giustino, Phys. Rev. Lett. **115**, 176401 (2015).
[51] J. Sjakste, N. Vast, M. Calandra, and F. Mauri, Phys. Rev. B **92**, 054307 (2015).
[52] S. Asanabe, J. Phys. Soc. Jpn. **14**, 281 (1959).
[53] H. Maier and D. R. Daniel, J. Electron. Mater. **6**, 693 (1977).
[54] C. Julien, M. Eddrief, I. Samaras, and M. Balkanski, Mater. Sci. Eng. B **15**, 70 (1992).
[55] M. Lundstrom, *Fundametals of Carrier Transport* (Cambridge University Press, Cambridge, UK, 2000), pp. 139–141.
[56] Y. K. Lee, K. Ahn, J. Cha, C. Zhou, H. S. Kim, G. Choi, S. I. Chae, J.-H. Park, S.-P. Cho, S. H. Park, Y.-E. Sung, W. B. Lee, T. Hyeon, and I. Chung, J. Am. Chem. Soc. **139**, 10887 (2017).
[57] A. Dewandre, O. Hellman, S. Bhattacharya, A. H. Romero, G. K. H. Madsen, and M. J. Verstraete, Phys. Rev. Lett. **117**, 276601 (2016).
[58] T. H. Patel, R. Vaidya, and S. G. Patel, Bull. Mater. Sci. **26**, 569 (2003).
[59] X. Guan, P. Lu, L. Wu, L. Han, G. Liu, Y. Song, and S. Wang, J. Alloy. Compd. **643**, 116 (2015).
[60] G. K. Madsen and D. J. Singh, Comput. Phys. Commun. **175**, 67 (2006).
[61] P. Sun, B. Wei, J. Zhang, J. M. Tomczak, A. Strydom, M. Sondergaard, B. B. Iversen, and F. Steglich, Nat. Commun. **6**, 7475 (2015).
[62] A. F. May, D. J. Singh, and G. J. Snyder, Phys. Rev. B **79**, 153101 (2009).